Available online at www.sciencedirect.com
SCIENCE DIRECT®
International Journal of Heat and Fluid Flow 26 (2005) 307–321
International Journal of HEAT AND FLUID FLOW
www.elsevier.com/locate/ijhff

Unsteady natural convection in a triangular enclosure induced by surface cooling

Chengwang Lei *, John C. Patterson

School of Engineering, James Cook University, Townsville, QLD 4811, Australia

Received 15 December 2003; accepted 25 August 2004
Available online 28 October 2004

Abstract

This study considers the unsteady natural convection in a triangular domain induced by a constant cooling at the water surface. The study consists of two parts: a scaling analysis and numerical simulations. The scaling analysis for small bottom slopes reveals that three laminar flow regimes, namely conductive, transitional and convective flow regimes are possible depending on the Rayleigh number. Proper scales have been established to quantify the transient flow development in each of these flow regimes. The numerical simulation has verified the scaling predictions.

Keywords: Natural convection; Triangular enclosure; Convective instability; Scaling analysis

1. Introduction

The authors have previously investigated the unsteady natural convection in a triangular enclosure induced by the absorption of radiation through the water surface (Lei and Patterson, 2002c). In that study, we reported detailed scaling analysis with corresponding numerical simulations of the transient flow development in the enclosure subjected to a constant heating at the water surface. The present study considers an opposite process to the previously reported case, i.e. the unsteady natural convection in the triangular enclosure subjected to a constant cooling at the water surface. Both studies have been motivated by the interest in understanding the heat transfer and exchange of nutrients or pollutants from the coastal region to the interior waters of lakes or reservoirs. The heating and cooling through the water surface form a complete diurnal forcing cycle, to which real lakes and reservoirs are always subjected.

A considerably large number of investigations have been reported in the literature on the fluid dynamics of nearshore lake waters, reservoir sidearms or other shallow water bodies with a sloping bottom. Among the early investigations, Adams and Wells (1984) and Monismith et al. (1990) monitored the temperature structures and velocity profiles in the sidearms of a lake and a reservoir in consecutive days (multiple diurnal cycles); Horsch and Stefan (1988) and Horsch et al. (1994) carried out a simple model experiment and a series of two dimensional simulations to model the night-time cooling in littoral waters; Farrow and Patterson (1994) and Lei and Patterson (2002a,b,c) have investigated the corresponding daytime heating process. The unsteady forcing during a diurnal cycle has been considered by Farrow and Patterson (1993a) which provided an asymptotic solution to the flow based on the assumption of small bottom slope. Farrow and Patterson (1993b) and Lei and Patterson (2003) have also investigated the instability issues surrounding the daytime heating process.

* Corresponding author. Tel.: +61 7 4781 4172; fax: +61 7 4775 1184.
E-mail addresses: chengwang.lei@jcu.edu.au (C. Lei), john.patterson@jcu.edu.au (J.C. Patterson).

0142-727X/$ - see front matter © 2004 Elsevier Inc. All rights reserved.
doi:10.1016/j.ijheatfluidflow.2004.08.010

Notation

A	bottom slope, $A = h/L$
B	buoyancy flux at water surface (m^2/s^3)
C_p	specific heat (J/kg K)
g	acceleration due to gravity
Gr	Grashof number, $Gr = g\beta H_0 h^4/(\nu^2 k)$
H, H_m	horizontal heat transfer rates
H_0	volumetric cooling intensity at water surface (m K/s), $H_0 = I_0/(\rho_0 C_p)$
I_0	rate of heat loss at water surface (W/m^2)
k	thermal diffusivity (m^2/s)
l	horizontal length of cooling
L, h	length and depth of the wedge
n	constant or coordinate normal to the bottom
N	Brunt–Vaisala frequency
p	pressure
Pr	Prandtl number, $Pr = \nu/k$
Q, Q_m	exchange flow rates
Ra	Rayleigh number, $Ra = g\beta H_0 h^4/(\nu k^2)$
Ra_c	critical Rayleigh number
t	time
t_B, t_c	time scales for thermal instability and steady state of thermal boundary layer
t_d, t_L	time scales for diffusion of heat flux over depth and length of the domain
t_i, t_m	time scales for switch of flow mechanisms
T, T_0	temperature and initial water temperature
$\overline{T}$	spatially averaged temperature
T_s	temperature scale in surface layer
u, v	velocity components in x and y directions
u_b, u_s	velocity scales in bottom and surface layers due to Phillips mechanism
x, y	coordinates in horizontal and vertical directions

Greeks

β	coefficient of thermal expansion (1/K)
δ_b, δ_s	thickness of bottom and surface layers
$\Delta T/L_y$	temperature gradient in stratified fluid
ν	kinematic viscosity (m^2/s)
ρ_0	density (kg/m^3)
θ	inclination angle of sloping bottom
τ	temperature variation

Subscripts

x, y, z	partial derivatives with respect to a spatial direction
t	partial derivatives with respect to time

More recently, Farrow (2004) extended the asymptotic results of Farrow and Patterson (1993a) for the diurnal cycle to include arbitrary bottom geometry.

It is now understood that the horizontal exchange flows in coastal waters of lakes or reservoirs are driven by imposed horizontal temperature gradients as a consequence of unequal heat capture during the day or unequal heat loss at night, both resulting from a varying water depth. Put simply for the day-time case, in the shallow parts the vertically averaged volumetric rate of absorption of a spatially uniform incident radiation flux is greater than in the deeper parts, resulting in relatively warm shallow regions when compared with the deep regions. A convectively driven circulation results, with a warm outflow along the surface and a cool return flow up the slope. A similar but converse argument may be made for the night-time cooling condition. The primary circulation generated by the above mechanism may also be complicated by the flow instabilities existing during the entire diurnal cycle.

One of the objectives of investigations on the related topics is to establish proper scales to quantify the horizontal exchange flows in coastal waters. This has practical significance. For the daytime heating process, Lei and Patterson (2002c) have provided detailed scales for the transient flow development in a shallow wedge with a small bottom slope. Their scaling analysis assumed initially isothermal and stationary conditions and a constant incident radiation at the water surface. The scaling has revealed three possible flow regimes, namely conductive, transitional and convective flow regimes, depending on the Rayleigh number (Ra). Attempts have also been made to quantify the exchange flow for the corresponding cooling process. Based on a series of numerical simulations, Horsch and Stefan (1988) proposed that the circulation flow rate in littoral waters subjected to a constant cooling at the water surface was proportional to $Ra^{1/n}$, where $2 < n < 3$. However, no detailed analysis with respect to this scale was reported and no other scales for quantifying the flow were established in that study. Sturman et al. (1999) reinvestigated the flow rate scale proposed by Horsch and Stefan (1988) for the steady flow case and claimed that the exchange flow rate was better described by $0.24B^{1/3}(l\tan\theta/(1+\tan\theta))^{4/3}$. The transient features of the unsteady flow development were not considered in Sturman et al. (1999).

The present study is aimed at establishing various scales to quantify the unsteady natural convection in coastal waters during the night-time cooling case with a constant cooling flux at the water surface. This is achieved through combined analytical and numerical

procedures. First, a scaling analysis is carried out to quantify the transient flow development, and then a series of numerical simulations are conducted to verify the scaling results. The present scaling analysis carries similar assumptions as the previous analysis for the heating process (Lei and Patterson, 2002c), i.e. the flow in the wedge is initially isothermal and stationary, the cooling at the water surface is uniform, and the bottom slope is very small.

The rest of this paper is arranged as follows: the details of the problem description and scaling procedures are given in Section 2, whereas the details of the numerical procedures are given in Section 3. Section 4 presents the results obtained from the numerical simulations with comparisons to the scaling predictions. Finally, Section 5 summarizes the present investigation.

2. Formulation and scaling

We consider a two-dimensional wedge of length L and maximum depth h with rigid non-slip boundaries at the bottom and end and an open boundary at the top (see Fig. 1). The bottom slope is defined as $A = h/L$. The wedge is filled with water initially at rest and at temperature T_0. At time $t = 0$, a surface cooling of intensity I_0 is applied instantaneously and thereafter maintained.

The water temperature in the enclosure decreases as a consequence of the heat loss through the surface. The subsequent flow and temperature changes within the wedge are then governed by the Navier–Stokes equations and energy equation. The two-dimensional forms of the governing equations are written as follows, in which the Boussinesq assumptions have been made:

$$u_t + uu_x + vu_y = -\rho_0^{-1}p_x + \nu\nabla^2 u \tag{1}$$

$$v_t + uv_x + vv_y = -\rho_0^{-1}p_y + \nu\nabla^2 v + g\beta(T - T_0) \tag{2}$$

$$T_t + uT_x + vT_y = k\nabla^2 T \tag{3}$$

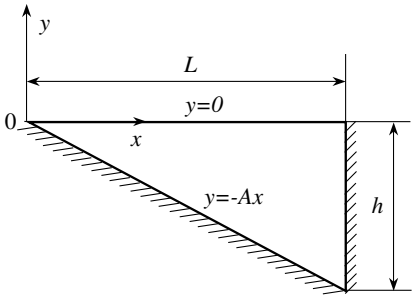

Fig. 1. Geometry of the flow domain.

$$u_x + v_y = 0 \tag{4}$$

where the fluid properties β, ρ_0, ν and k are evaluated at the reference temperature (T_0).

The boundary conditions for velocity and temperature are described as follows:

(i) On the water surface (i.e. $y = 0$), the heat loss is quantified by a heat flux condition as

$$T_y = -H_0/k \tag{5}$$

where $H_0 = I_0/(\rho_0 C_p)$, and C_p is evaluated at the reference temperature. It is also assumed that the water surface is stress-free ($\partial u/\partial y = 0$ and $v = 0$). The stress-free surface condition is compatible with the field condition in geophysical applications. Similar results are expected if a non-slip condition is specified on the top boundary. This has been demonstrated in the earlier numerical simulations of Horsch and Stefan (1988), in which both stress-free and non-slip boundary conditions were tested.

(ii) On the sloping bottom ($y = -Ax$), rigid non-slip velocity conditions ($u = v = 0$) apply. The sloping bottom is also insulated, i.e. $\partial T/\partial n = 0$, where n is the direction normal to the sloping bottom.

(iii) The boundary conditions on the end wall at $x = L$ are similar to those on the sloping bottom, i.e. rigid non-slip conditions for the velocity ($u = v = 0$) and insulated condition for the temperature ($\partial T/\partial x = 0$).

2.1. Development of the primary circulation

2.1.1. Growth of the surface layer

Initially, there is no flow and no heat conduction in the enclosure. As soon as the surface cooling starts, a thermal layer starts to grow downwards underneath the water surface. The water temperature in this surface layer drops due to the heat loss through the surface. From the temperature boundary condition (5) for the water surface, a scale for the temperature drop in the surface layer is obtained:

$$T_s \sim H_0\delta_s/k \tag{6}$$

where T_s is the scale for the temperature variation in the surface layer relative to the bulk temperature in the inner region and δ_s is the thickness of the surface layer. A balance between the unsteady and diffusion terms in the energy equation (3) yields a scale for the thickness of the surface layer

$$\delta_s \sim (kt)^{1/2} \tag{7}$$

Using (7), the temperature variation scale in the surface layer becomes

$$T_s \sim H_0(t/k)^{1/2} \sim (kt/h^2)^{1/2}H_0h/k \tag{8}$$

2.1.2. Inception of the circulation

Since the water surface is subjected to uniform cooling, the heat loss through the surface does not generate a horizontal temperature gradient directly, but causes a vertical stratification in the surface layer. This stratification is potentially unstable. At early time, the destabilising stratification is too weak to cause any instability, and thus no flow is resulted directly from the surface cooling. However, there are two mechanisms that may drive a flow in the wedge, both being associated with the growth of the surface layer.

The first driving mechanism is the Phillips mechanism described in Phillips (1970) and Wunsch (1970). The application of this mechanism to the surface cooling case in a triangular domain is described in Horsch and Stefan (1988). In brief, the uniform heat loss through the water surface creates horizontal and parallel isotherms over almost the entire length of the surface layer. In the shallow end, however, the horizontal isotherms must curl over to become perpendicular to the sloping bottom in order to satisfy the no-flux condition there. This process creates an additional boundary layer near the sloping bottom, in which a horizontal temperature gradient is established, which in turn drives a flow down the slope.

The other driving mechanism, which is also related to the diffusion of the surface heat flux and the topographical nature of the wedge, is referred to as unequal heat loss. Since the water depth varies continuously from the shallow end to the deep end, the time scale for the diffusion of the surface heat flux over the local water depth is a function of the horizontal location. In the region near the tip, the surface flux rapidly diffuses to the bottom, resulting in approximately vertical isotherms in this region. It is expected that the region with vertical isotherms will gradually expand toward the deep part of the wedge while the surface cooling is maintained. The nearly vertical isotherms may be interpreted as the surface heat flux being uniformly distributed over the local depth of the water column. Since the water depth is the smallest near the tip, this region is cooled the most. Therefore, a horizontal temperature gradient is established in the shallow region, which in turn drives a large-scale circulation within the wedge.

Fig. 2 presents typical temperature structures at early times obtained from a numerical simulation, from which

Fig. 2. Typical temperature structures at early stages of the flow development. Plotted here are the calculated temperature contours for $Pr = 7$, $Gr = 10^5$ and $A = 0.1$ at the dimensionless time $t = 0.02$. The dimensionless contour interval is 0.04.

both mechanisms mentioned above can be identified. In the subsequent text, the flows resulting from both mechanisms are discussed and compared.

(a) Flow driven by the Phillips mechanism

As mentioned above, an additional boundary layer is created as a consequence of the curling over of the horizontal isotherms near the sloping bottom. To distinguish this boundary layer from the surface layer, we refer to it as the bottom layer. The thickness of the bottom layer is denoted by δ_b. Wunsch (1970) has provided a scale for the thickness of the bottom layer in a stably stratified fluid:

$$\delta_b \sim (\nu k)^{1/4}/N^{1/2} \tag{9}$$

where N is the Brunt–Vaisala frequency given by

$$N = (g\beta\Delta T/L_y)^{1/2} \tag{10}$$

and $\Delta T/L_y$ represents the vertical temperature gradient in the stratified fluid. In the present case, the stratification exists in the surface layer only and is over a length scale of $O(\delta_s)$. Therefore, $\Delta T/L_y \sim T_s/\delta_s \sim H_0/k$. Using this in (10), we have

$$N \sim (g\beta H_0/k)^{1/2} \tag{11}$$

Substitution of (11) into (9) yields

$$\delta_b \sim (\nu k^2/g\beta H_0)^{1/4} \sim Ra^{-1/4}h \tag{12}$$

where Ra is the Rayleigh number given by $Ra = PrGr$, and Pr and Gr are respectively the Prandtl number and Grashof number defined below:

$$Pr = \nu/k \tag{13}$$

$$Gr = g\beta H_0 h^4/\nu^2 k \tag{14}$$

It is seen from (12) that the thickness of the bottom layer is constant, depending only on the global Rayleigh number of the flow. It is assumed in the present study that the inclination angle of the bottom is very small, i.e. $A \ll 1$, which is typical in geophysical situations. With this assumption, δ_b is approximately the vertical length scale for the bottom layer. The small-slope assumption also implies that the horizontal component of the flow velocity approximately represents the flow velocity along the slope, while the vertical component of the flow velocity is negligible. Since the temperature gradient in the bottom layer acts to accelerate the flow within the entire domain, an appropriate horizontal length scale for the bottom layer is $L(= h/A)$, i.e. the length of the wedge.

The temperature scale for the bottom layer is identical to that for the surface layer. A balance between the pressure gradient and buoyancy terms in Eq. (2) yields a scale for the pressure in the bottom layer

$$p/\rho_0 \sim g\beta T_s\delta_b \tag{15}$$

Assume the velocity scale in the bottom layer driven by the Phillips mechanism is u_b. In Eq. (1), the unsteady inertia term is $O(u_b/t)$, the advection term is $O(u_b^2/L)$, and the viscous term is $O(\nu u_b/\delta_b^2)$. The ratio of the advection term to the unsteady inertia term is $O(u_b t/L)$. For small enough time t, $u_b t < L$, and thus the advection term is insignificant when compared with the unsteady inertia term. The ratio of the unsteady inertia term to the viscous term is

$$(u_b/t)/(\nu u_b/\delta_b^2) \sim \delta_b^2/\nu t \sim (PrRa^{1/2})^{-1}h^2/kt \tag{16}$$

The above comparison yields a time scale for the switch from an inertia-dominated bottom layer to a viscosity-dominated bottom layer, which is given by

$$t_i \sim (PrRa^{1/2})^{-1}h^2/k \tag{17}$$

For $t < t_i$, the inertia term dominates the viscosity term, whereas for $t > t_i$, the reverse is true.

The velocity scale in the bottom layer is then obtained from Eq. (1). For $t < t_i$, a balance between the inertia term and the pressure gradient term yields

$$u_b \sim \rho_0^{-1}(p/L)t \sim APrRa^{3/4}(kt/h^2)^{3/2}k/h \tag{18}$$

and for $t > t_i$, a balance between the viscous term and the pressure gradient term yields

$$u_b \sim \rho_0^{-1}(p/L)(\delta_b^2/\nu) \sim ARa^{1/4}(kt/h^2)^{1/2}k/h \tag{19}$$

The downwelling flow in the bottom layer is fed by the inflow (moving toward the tip) in the surface layer by changing its direction near the tip. The conservation of mass requires

$$u_b\delta_b \sim u_s\delta_s \tag{20}$$

where u_s is the velocity scale in the surface layer resulting from the Phillips mechanism. The corresponding velocity scale in the surface layer can be obtained as

$$u_s \sim APrRa^{1/2}(kt/h^2)k/h \quad (t < t_i) \tag{21}$$

$$u_s \sim Ak/h \sim k/L \quad (t > t_i) \tag{22}$$

Eq. (22) indicates that u_s is constant for $t > t_i$ and the maximum velocity in the surface layer due to the Phillips mechanism is of the order of k/L, provided that the surface layer is growing on the scale given by (7).

(b) Flow driven by unequal heat loss

The second driving mechanism is associated with a region near the tip which has approximately vertical isotherms. In this case, the heat loss through the water surface is considered to be uniformly distributed over the local depth. Therefore, the energy equation for this region can be rewritten as

$$T_t + uT_x + vT_y = k\nabla^2 T - H_0/Ax \tag{23}$$

In the above equation, the second term on the right-hand side quantifies the averaged heat loss over the local water column with Ax being the local water depth. Since this particular region is associated with the diffusion of the surface heat flux or the growth of the surface layer, the maximum water depth for this region is the same order of the thickness of the surface layer, and thus an appropriate vertical length scale for this region is $\delta_s \sim (kt)^{1/2}$. The initial energy balance in this region is between the unsteady term and the sink term, which gives a temperature scale for this region

$$T \sim H_0 t/Ax \sim H_0 t/\delta_s \sim (kt/h^2)^{1/2}H_0 h/k \tag{24}$$

Again, T represents the temperature variation in the surface layer relative to the bulk temperature in the domain. The above temperature scale is identical to the scale given by (8).

The horizontal temperature gradient in the tip region establishes a horizontal pressure gradient that drives a flow into the tip. Since the horizontal pressure gradient acts to accelerate the flow over the entire length of the surface layer, an appropriate horizontal length scale for the pressure gradient is L. A balance between the pressure gradient and buoyancy terms in the vertical momentum equation (2) yields a scale for the pressure

$$p/\rho_0 \sim g\beta T\delta_s \sim g\beta H_0 t \tag{25}$$

In the horizontal momentum equation (1), the unsteady inertia term is $O(u/t)$, the advection term is $O(u^2/L)$, and the viscous term is $O(\nu u/\delta_s^2)$. The ratio of the advection term to the unsteady inertia term is $O(ut/L)$. For small enough time t, $ut < L$, and thus the advection term is insignificant when compared with the unsteady inertia term. The ratio of the unsteady inertia term to the viscous term is $O(Pr^{-1})$. The present scaling analysis considers only flows with a Prandtl number greater than unity. For $Pr > 1$, the viscous term dominates the unsteady inertia term. Hence, the correct momentum balance in the horizontal direction is between the pressure gradient and the viscous terms, which then yields a velocity scale in the surface layer

$$u \sim ARa(kt/h^2)^2 k/h \tag{26}$$

(c) Comparison of the flows driven by two different mechanisms

Now that the velocity scales in the surface layer driven by both mechanisms have been obtained, the relative importance of these two mechanisms can be compared. The comparison shows that for $t < t_m$, where t_m is given by

$$t_m \sim Ra^{-1/2}h^2/k \tag{27}$$

$u_s > u$, and thus the Phillips mechanism dominates the unequal heat loss. For $t > t_m$, the reverse is true. Therefore, t_m is the time scale for the switch from the first mechanism to the second mechanism. Clearly, $t_m > t_i$ for $Pr > 1$. Examination of the time scale t_m indicates that for small Rayleigh numbers, t_m is large and

therefore the Phillips mechanism is important for a significant period of time. This applies to the cases with very weak surface cooling in which the flow is dominated by adjustment at the sloping boundary of the induced stratification as described by Phillips (1970) and Wunsch (1970). On the contrary, t_m becomes small if the Rayleigh number is large. In this case, the Phillips mechanism dominates only for a limited time. In geophysical situations with night-time surface cooling, the Rayleigh number is normally quite large, and thus the contribution of the Phillips mechanism can be ignored. In the subsequent analysis, only the contribution from the unequal heat loss is considered.

2.1.3. Steady state of the boundary layer

While the surface layer is growing due to the heat loss through the water surface, heat is also being convected from the inner layer into the surface layer by the velocity (26). The surface layer will continue to grow downward until the heat loss through the surface is balanced by that convected into this layer. In the early stage, the convective term of Eq. (23) is $O(uT/L)$ and the conduction term is $O(kT/\delta_s^2)$. Using (7) and (26), a balance between the convection and conduction terms yields a growth time scale for the surface layer

$$t_c \sim (A^2 Ra)^{-1/3} h^2/k \tag{28}$$

It is interesting to note that the above time scale for the steady state is identical to the steady state time scale for the heating case discussed in Lei and Patterson (2002c) although different flow mechanisms are involved in the heating and cooling problems. At $t \sim t_c$, the length, temperature and velocity scales for the surface layer have become

$$\delta_s \sim (A^2 Ra)^{-1/6} h \tag{29}$$

$$T \sim (A^2 Ra)^{-1/6} H_0 h/k \tag{30}$$

$$u \sim (A^{-1} Ra)^{1/3} k/h \tag{31}$$

It is noteworthy that the temperature scale given by (30) represents the temperature variation in the surface layer relative to the bulk temperature in the domain. It does not include any change of the bulk temperature with time (see Section 3.1 for details). If $\delta_s \ll h$, the thermal boundary layer is distinct, which requires

$$Ra > A^{-2} \tag{32}$$

2.2. Onset of the thermal layer instability

As noted previously, the stratification in the surface layer is potentially unstable. If the growth of the surface layer reaches a critical point, the instability will set in. The instability characteristics of an inclined layer along the sloping bottom have been discussed in detail in Lei and Patterson (2002c). Similar analysis may be carried out for the horizontal surface layer in the present case. For brevity, the details are not given here. Following the procedures outlined in Lei and Patterson (2002c), a critical time scale for the onset of thermal layer instability at a given Rayleigh number is obtained

$$t_B \sim (Ra_c/Ra)^{1/2} h^2/k \tag{33}$$

where $Ra_c \approx 657.5$. For $t < t_B$, the surface layer is stable, and for $t \geqslant t_B$, the instability will set in. The scale (33) indicates that the critical time for the onset of convective instability in the surface layer increases as the Rayleigh number decreases. Theoretically, t_B approaches infinity if $Ra \to 0$. However, as demonstrated later, for Rayleigh numbers below a critical value the instability will never occur irrespective of the cooling time.

Similar to the heating case (Lei and Patterson, 2002c), two important time scales have been obtained for the surface layer; first, the time scale for the growth of the surface layer (t_c given by (28)), and second, the time scale for the onset of the convective instability (t_B given by (33)). Comparisons of these two time scales with t_m, the time scale for the switch from the first mechanism to the second mechanism, show that $t_B \gg t_m$ always holds and $t_c > t_m$ if $Ra > A^4$. Since $A \ll 1$, the above comparison is equivalent to $t_c > t_m$ if $Ra > 0$. Therefore, $t_c \gg t_m$ holds in the present analysis. This demonstrates from another point of view that the effect of the Phillips mechanism to the overall flow development may be ignored.

The actual flow property of the surface layer now depends on the comparison of t_c and t_B, which is given by

$$t_c/t_B \sim (Ra/A^4 Ra_c^3)^{1/6} \tag{34}$$

Therefore, for

$$Ra > A^4 Ra_c^3 \tag{35}$$

$t_c > t_B$, and the convective instability sets in before the growth of the surface layer ceases. On the other hand, if $Ra < A^4 Ra_c^3, t_c < t_B$, the surface layer reaches steady state before the convective instability is possible, and the layer is therefore always stable.

2.3. Possible flow regimes and major flow features

Similar to the analysis of the heating case (Lei and Patterson, 2002c), the natural convection flow in the wedge subjected to surface cooling can be classified into different flow regimes depending on the Rayleigh number and the relative order of (32) and (35). Since Ra_c is approximately constant in this case (≈ 657.5), the comparison between the scales (32) and (35) relies mostly on the bottom slope A. There are two possibilities, i.e. $A^{-2} > A^4 Ra_c^3$ and $A^{-2} < A^4 Ra_c^3$, which are equivalent to the conditions $A < Ra_c^{-0.5}$ and $A > Ra_c^{-0.5}$.

Therefore, the dividing bottom slope is $A \sim 0.039$. In the following discussions, only the latter case with $A > Ra_c^{-0.5}$ is considered. Readers may refer to Lei and Patterson (2002c) for discussions regarding the other case with $A < Ra_c^{-0.5}$ (very small bottom slopes).

In the case with $A > Ra_c^{-0.5}$, the bottom slope may play a significant role. However, the present analysis still follows the assumption of $A \ll 1$. The relative order of the criteria (32) and (35) becomes $A^{-2} < A^4 Ra_c^3$ and thus the laminar convective flow may be classified into the following three flow regimes depending on the global Rayleigh number:

2.3.1. Conductive regime ($Ra < A^{-2} < A^4 Ra_c^3$)

For $Ra < A^{-2} < A^4 Ra_c^3$, the flow is stable to the Rayleigh–Bénard instability. The surface layer grows steadily, and it encompasses the entire domain before convection becomes important. The time scale for the diffusion of the boundary heat flux over the depth is

$$t_d \sim h^2/k \tag{36}$$

For $t > t_d$, heat conduction over the depth will cease. Instead, horizontal heat conduction will dominate due to the existence of a horizontal temperature gradient as a consequence of the topographic effect. The time for the flow to reach a final steady state will be the temperature diffusion time scale over the length of the domain, which is

$$t_L \sim L^2/k \sim A^{-2}h^2/k \sim A^{-2}t_d \tag{37}$$

This flow regime is classified as a conductive regime with conduction dominating the heat transfer in both transient and steady states. At the steady state, the temperature profile in the enclosure will become close to vertically uniform, and the horizontal heat transfer will be dominated by conduction.

2.3.2. Transitional regime ($A^{-2} < Ra < A^4 Ra_c^3$)

For $A^{-2} < Ra < A^4 Ra_c^3$, the flow is again stable to the Rayleigh–Bénard instability. A distinct surface layer is established under the water surface, and it reaches a steady state prior to the onset of the convective instability. Since the flow in the surface layer moves toward the tip, when it reaches the tip region it has no other choice but to change its direction and discharge into the core region. The core region is initially isothermal, and thus the discharge of the cold surface layer forms a buoyancy current flowing down the slope. Applying similar procedures to those provided in Lei and Patterson (2002c) for an intrusion layer in a heated triangular domain, the relevant scales including thickness, velocity and growth time for the buoyancy current can be obtained. It is found that these scales are identical to those of the surface layer, and thus both the surface layer and the buoyancy current reach their steady states at the same time. At the steady state, the velocity of the primary circulation is quantified by (31), and the horizontal exchange rate in coastal waters (the volumetric flow rate) can be approximated by

$$Q \sim (uh)/2 \sim (Ra/8A)^{1/3}k \tag{38}$$

The above scale agrees well with the previously reported results in terms of the Rayleigh number dependence (Horsch and Stefan, 1988; Sturman et al., 1999).

In the transitional regime, both conduction and convection participate in the heat transfer.

2.3.3. Convective regime ($Ra > A^4 Ra_c^3 > A^{-2}$)

For $Ra > A^4 Ra_c^3 > A^{-2}$, the surface layer is still distinct, but unstable to the Rayleigh–Bénard instability. The convective instability sets in before the growth of the thermal boundary layer is completed. The development of the surface layer in the early stage (for $t < t_B$) is quantified by the scales (7), (8) and (26). At the time t_B, the surface layer becomes unstable to the Rayleigh–Bénard instability and the instability sets in. The expected form of the thermal layer instability will be descending cold-water plumes. However, the actual pattern as well as other features of the secondary convection depends on the Rayleigh number and other flow conditions, and is out of the scope of the present investigation. The subsequent flow development cannot be quantified by a simple scaling analysis. Readers may refer to Lei and Patterson (2002c) for a qualitative description of the flow process after the onset of the thermal layer instability. Depending on the Rayleigh number, either a steady or a quasi-steady flow may result in the end. The heat transfer in this flow regime is dominated by convection.

It is worth noting that the above flow regimes for the surface cooling induced natural convection flow in the wedge are identical to those revealed for the heating case due to absorption of radiation (Lei and Patterson, 2002c). The critical Rayleigh numbers dividing different flow regimes as well as the major flow features in each flow regime are also similar. The similarity between heating and cooling cases will be demonstrated further through numerical simulations.

3. Numerical procedures

A series of two-dimensional numerical simulations are conducted in order to validate the previous scaling analysis and obtain a better understanding of the flow features in different flow regimes. For the convenience of numerical calculations, the governing equations are first simplified with a quasi-steady state assumption, and then normalised with appropriate scales. The numerical procedures applied in this study are similar to those described in Lei and Patterson (2002a,c, 2003), and thus only a brief summary is given below.

Following the quasi-steady state assumption described in Lei and Patterson (2002a,c, 2003), the temperature change in the wedge is split into two components:

$$T - T_0 = \overline{T}(t) + \tau(x, y, t) \tag{39}$$

i.e. a spatially averaged temperature, $\overline{T}(t)$, which decreases in time, and a spatial variation of temperature, $\tau(x, y, t)$, which has a steady state spatial distribution after a transition. The spatially averaged temperature is obtained from an energy balance, which gives $\overline{T}(t) = -(2H_0/h)t$, a linear decrease with time.

Substituting Eq. (39) into Eqs. (2) and (3) yields the following equations with respect to τ

$$v_t + uv_x + vv_y = -\rho_0^{-1}p_y + v\nabla^2 v + g\beta(\overline{T} + \tau) \tag{40}$$

$$\tau_t + u\tau_x + v\tau_y = k\nabla^2\tau + 2H_0/h \tag{41}$$

With the Boussinesq assumptions for buoyancy made, the spatially averaged temperature $\overline{T}(t)$ can be included in the background pressure and therefore neglected in Eq. (40). The same boundary conditions apply for τ as for T. The complete system equations now consist of Eqs. (1), (40), (41) and (4) with the spatially averaged temperature $\overline{T}(t)$ dropped from Eq. (40).

The quantities in the governing equations are then normalised with the following scales: the length scale $x, y \sim h$; the time scale: $t \sim h^2/k$; the temperature scale: $\tau \sim H_0 h/k$; the velocity scale: $u, v \sim k/h$; and the pressure scale: $\rho_0^{-1}p_x, \rho_0^{-1}p_y \sim g\beta H_0 h/k$. The non-dimensional form of the complete governing equations is now written as:

$$u_t + uu_x + vu_y = -(Pr^2 Gr)p_x + Pr\nabla^2 u \tag{42}$$

$$v_t + uv_x + vv_y = -(Pr^2 Gr)p_y + Pr\nabla^2 v + (Pr^2 Gr)\tau \tag{43}$$

$$\tau_t + u\tau_x + v\tau_y = \nabla^2\tau + 2 \tag{44}$$

$$u_x + v_y = 0 \tag{45}$$

All the quantities in Eqs. (42)–(45) are now dimensionless. The governing equations in the dimensionless form are then solved using a finite difference method. Details of the numerical schemes are described in Lei et al. (2000).

4. Results and discussion

Again, following the practice in Lei and Patterson (2002a,c), two parameters that have practical significance are defined here for the discussion of the numerical results: the average volumetric flow rate and the average horizontal heat transfer rate:

$$Q_m = L^{-1}\int_0^L Q(x)\,dx, \quad \text{where } Q(x) = 0.5\int_{-Ax}^0 |u|\,dy \tag{46}$$

$$H_m = L^{-1}\int_0^L H(x)\,dx, \quad \text{where } H(x) = \int_{-Ax}^0 (u\tau - \tau_x)\,dy \tag{47}$$

In the above equations, $Q(x)$, Q_m and $H(x)$, H_m have been normalised using the scales k and $I_0 h$ respectively, and all quantities are dimensionless. It is seen from the above definitions that the horizontal heat transfer rate takes into account the contributions of both convection and conduction.

Numerical solutions are now obtained with the aforementioned numerical procedures for a fixed bottom slope. A number of combinations of Prandtl and Grashof numbers, which spread over all three laminar flow regimes under the condition $Ra_c > A^{-2}$, are calculated. It is noteworthy that the boundary between adjacent flow regimes is not definite since a scaling factor applies to each scale as would be expected. All calculations are conducted in a triangular domain of a dimensionless length $L = 10$ and a depth of $h = 1$ (the bottom slope is $A = 0.1$).

To avoid a singularity at the tip in the numerical simulations, the tip is cut off at $x = 0.16$, and an extra rigid non-slip and adiabatic wall boundary is assumed there. The impact of this geometry modification on the overall flow development can be estimated based on the previous scaling. As noted earlier, both driving mechanisms of the global circulation are relevant to the growth of the surface layer and the topographical effect of the sloping bottom. However, with the modified geometry, the topographical effect is insignificant before the growth of the surface layer goes beyond the water depth at the tip (i.e. $Ax = 0.016$), and thus the global flow at the early stage is negligible. The time scale for the surface layer to grow beyond the water depth Ax can be estimated using (7) (normalised with relevant scales), which gives $t \sim (Ax)^2 = 2.56 \times 10^{-4}$. It will become clear later that this time scale is far before any features of the overall flow development become noticeable. Therefore, it is anticipated that the geometry modification mentioned above will not alter the overall flow development significantly.

A 111×41 non-uniform mesh (Mesh 1) is used for all the calculations presented later. To check the mesh and time-step dependence, two finer meshes (Meshes 2 and 3, see Table 1) are generated. All three meshes are then used to calculate the flow in the high Rayleigh number regime ($Ra > A^4 Ra_c^3$), which is the most sensitive to the refinement of mesh and time-step. For the calculations with Mesh 3, both the grid spacing and time step are halved from those for Mesh 1. Therefore, the CFL (Courant–Freidrich–Levy) number remains the same for the calculations with Meshes 1 and 3.

Fig. 3 plots the time histories of the calculated mean flow rates for two different Grashof numbers with all three meshes. It is clear in this figure that all solutions

Table 1
Parameters and results of mesh and time-step dependence test

Mesh	#1(111 × 41)	#2(166 × 61)	#3(221 × 81)	Maximum variation (%)
Time step	10^{-6}	0.5×10^{-6}	0.5×10^{-6}	
Results for Pr = 7, Gr = 10^5				
Flow rate	18.91	18.35	18.25	3.5
Heat transfer rate (%)	97.54	97.26	97.24	0.3
Results for Pr = 7, Gr = 10^6				
Flow rate	48.27	46.94	47.19	2.8
Heat transfer rate (%)	99.37	99.17	99.15	0.2

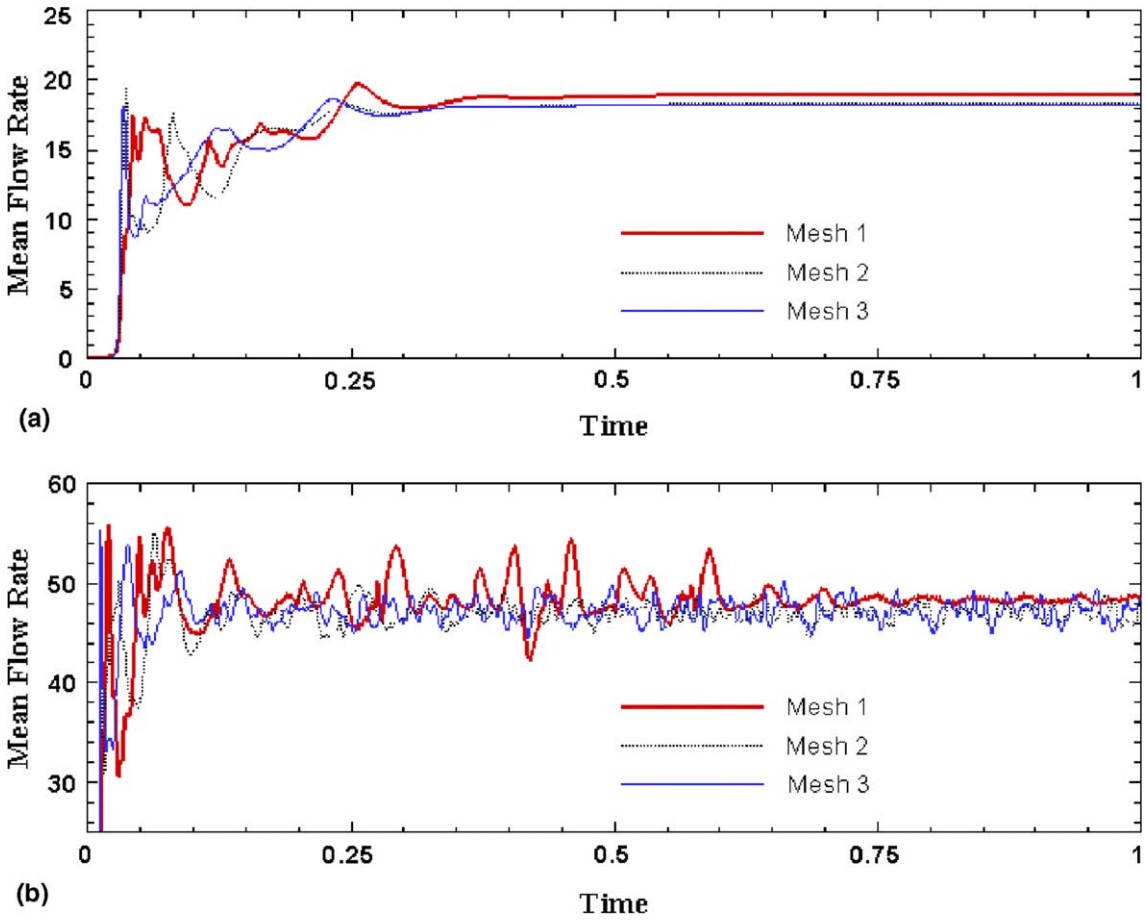

Fig. 3. Time histories of the mean flow rate (Eq. (46)) obtained with different meshes for $Pr = 7$ and (a) $Gr = 10^5$; (b) $Gr = 10^6$.

indicate three stages of the flow development, i.e. an initial growth stage, a transitional stage and a quasi-steady stage. At the initial growth stage, the solutions with different meshes follow closely to each other. However, the solutions diverge largely at the transitional stage. This is because the transitional stage is dominated by the occurrence of the convective instability, and the formation of convective cells is extremely sensitive to the grid resolution. At the steady/quasi-steady stage, similar solutions are obtained from different meshes. In the lower Grashof number case ($Gr = 10^5$), all three meshes generate a steady solution, whereas in the higher Grashof number case ($Gr = 10^6$), all three meshes give an oscillatory (quasi-steady) solution. The oscillation is due to the convective instability. Table 1 compares some selected quantities obtained with all meshes at the steady/quasi-steady state. Clearly, the two finer meshes (Meshes 2 and 3) produce almost identical solutions, and the variations between the coarsest mesh (Mesh 1) and the finer meshes are small. It is also expected that the variations are less significant at lower Rayleigh number values. Given that the purpose of the present study is to identify the flow mechanisms and major scales for the development of the flow rather than resolve the details of the convective instability, the discrepancy between the coarsest and finer meshes is tolerated. Therefore, Mesh

1 is used for the subsequent calculations. The time step used in this study is fixed at 10^{-6} for the convective flow regime and 2×10^{-6} for other flow regimes.

In the following sections, the major flow features in different flow regimes are summarized in Section 4.1; features of the horizontal heat transfer are discussed in Section 4.2; selected scales are validated in Section 4.3; and two important issues relevant to the numerical simulations are discussed in Section 4.4.

4.1. Flow structures in different flow regimes

As noted previously, the natural convection flow in a wedge subject to surface cooling may be classified into three different flow regimes that are identical to those for the corresponding heating case described in Lei and Patterson (2002c). The present numerical calculations also confirm that the flow structures in each flow regime are very similar to those in the heating case. Therefore, only the major flow features are briefly summarized below. Readers may refer to Lei and Patterson (2002c) for more detailed discussions of the flow structures in each of the three laminar flow regimes.

Fig. 4 plots the temperature contours and streamlines of different flow regimes at steady or quasi-steady state obtained for a fixed aspect ratio ($A = 0.1$) and a fixed Prandtl number ($Pr = 7$). It is seen that in the conductive flow regime ($Ra < A^{-2} < A^4 Ra_c^3$, Fig. 4a), the isotherms are approximately vertical. This is due to the fact that the surface layer expands downwards and eventually encompasses the entire domain, which results in a nearly uniform temperature profile over the local depth. With the existence of the bottom slope, a distinct horizontal temperature gradient is established across the enclosure, which maintains an extremely weak circulation at the steady state. In this flow regime, the primary circulation is featured by a stable single-cell structure.

In the transitional flow regime ($A^{-2} < Ra < A^4 Ra_c^3$, Fig. 4b), the isotherms near the shallow end are approximately vertical, indicating strong effect of conduction in this region. In the deep regions, the isotherms are tilted due to the convective effect. A comparison with the temperature structures presented in Lei and Patterson (2002c) for the heating case in the same flow regime shows that the isotherms are titled toward different directions in the present cooling case, suggesting that

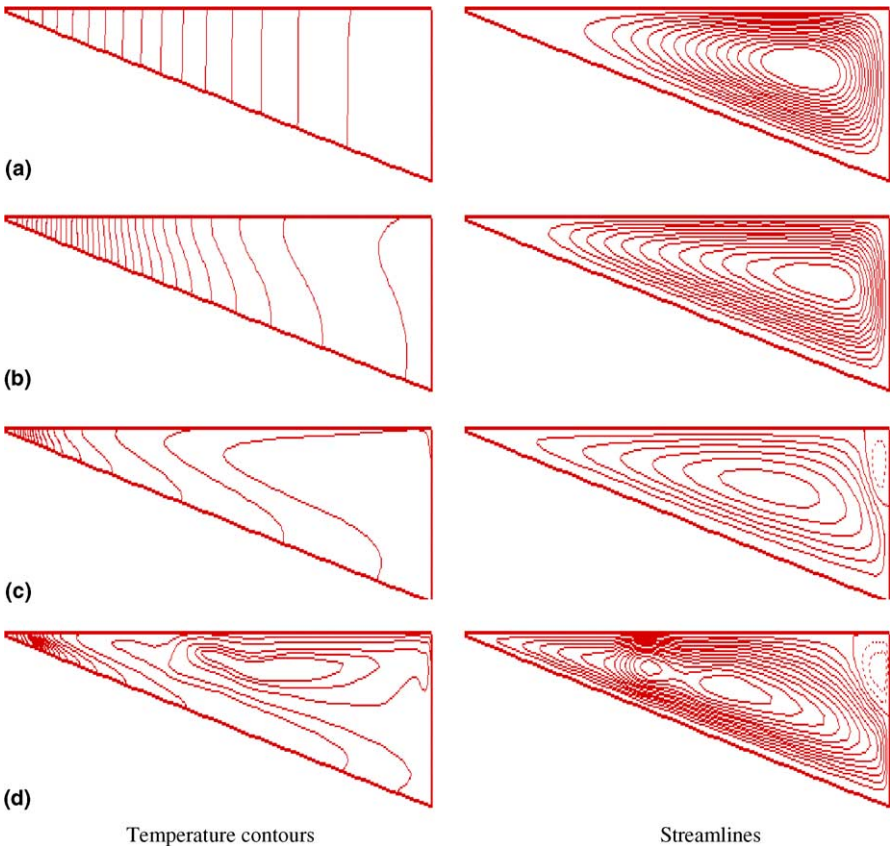

Fig. 4. Flow structures in different flow regimes at steady or quasi-steady state for $A = 0.1$ and $Pr = 7$. Figures on the left are temperature contours, and figures on the right are corresponding streamlines. The intensity of the primary circulation may be compared based on the maximum values of the stream function, which are given in parentheses below. (a) $Gr = 10$ (Conductive, 0.32); (b) $Gr = 500$ (Transitional, 3.9); (c) $Gr = 10^5$ at $t = 2.0$ (Convective, 33.2); (d) $Gr = 10^6$ at $t = 1.0$ (Convective, 78.0).

the convection is in the opposite direction to the heating case. As expected, the circulation becomes much stronger in this flow regime, but the streamlines still show a single closed cell.

Similar to the heating case (Lei and Patterson, 2002c), the flow development in the convective flow regime ($Ra > A^4 Ra_c^3 > A^{-2}$) passes through three distinct stages: an initial growth stage, a transitional stage and a quasi-steady stage. The start of the transitional stage is marked by the onset of the convective instabilities as a consequence of excessive cooling in the surface layer. The convective instabilities, which are seen in the form of descending thermals (cold-water plumes), break the single-cell circulation to form a cellular structure and accelerate the heat exchange between the surface layer and inner region. At a certain stage when the heat transfer through conduction is effectively balanced by the primary as well as the secondary convection, an equilibrium state is reached. The final flow structures in the convective flow regime depend on the Rayleigh number. At lower Rayleigh numbers, no secondary convection is observed at large times, and thus the flow becomes steady (Fig. 4c). However, for sufficiently high Rayleigh numbers, the secondary convection persists indefinitely, and the final flow is classified as quasi-steady (Fig. 4d).

4.2. Horizontal heat transfer in different flow regimes

The effects of Rayleigh number on heat transfer in the wedge may be seen from the calculated horizontal heat transfer rates (Eq. (47)), which are plotted in Fig. 5 for different flow regimes. In this figure, the contributions from conduction and convection as well as the total heat transfer rate are shown separately. Clearly, the heat transfer in the conductive flow regime is completely dominated by conduction in both the transient and steady states, whereas the contribution from convection is negligible (Fig. 5a). In the transitional regime, convection becomes increasingly significant as the Rayleigh number increases, and both conduction and convection participate in the heat transfer (Fig. 5b). It is interesting to note that the convective heat transfer exhibits a distinct peak at the early stage in this flow regime (Fig. 5b). The existence of this peak indicates an imbalance between the stronger inflow of cold water in the surface layer and the weaker outflow down the slope at the early stage. The time histories of the heat transfer rates calculated for the convective flow regime clearly confirm the three stages of the flow development discussed previously (see Fig. 5c and d). They also indicate strong flow instabilities at the transitional stage (Fig. 5c and d) and relatively weaker instabilities at the quasi-steady state for sufficiently high Rayleigh numbers (Fig. 5d). These flow instabilities are not seen at the final stage of the flow development for relatively lower Rayleigh numbers

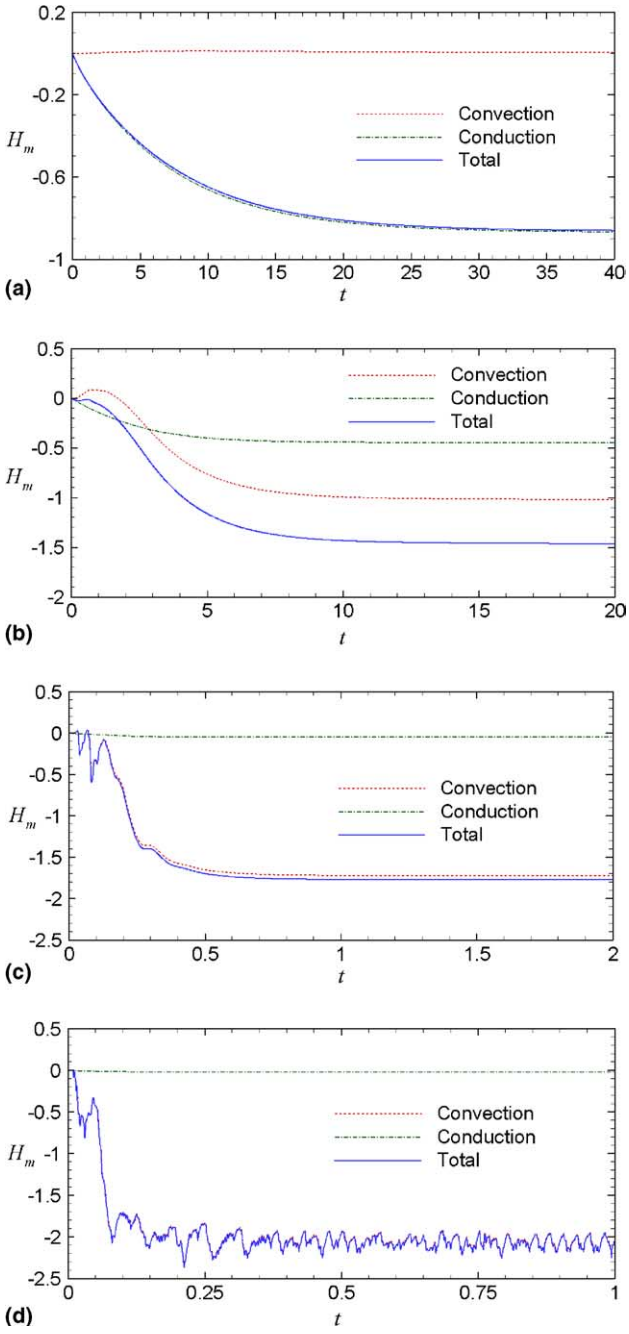

Fig. 5. Time history of the horizontal heat transfer rate for $A = 0.1$ and $Pr = 7$ in different flow regimes. (a) Conductive ($Gr = 10$); (b) transitional ($Gr = 500$); (c) convective ($Gr = 10^5$); (d) convective ($Gr = 10^6$).

(Fig. 5c). It is evident in Fig. 5c and d that the heat transfer in the convective flow regime is dominated by convection.

The dependence of the steady/quasi-steady state heat transfer rate on the Rayleigh number is shown in Fig. 6, which summarizes the numerical results obtained for two different Prandtl numbers ($Pr = 7$ and 70) and a range of Grashof numbers. Here, the heat transfer rates are normalized by the absolute value of the total heat

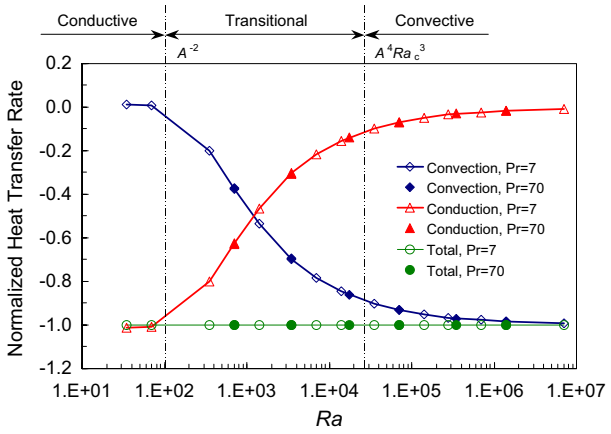

Fig. 6. Dependence of the steady state heat transfer rate on the Rayleigh number.

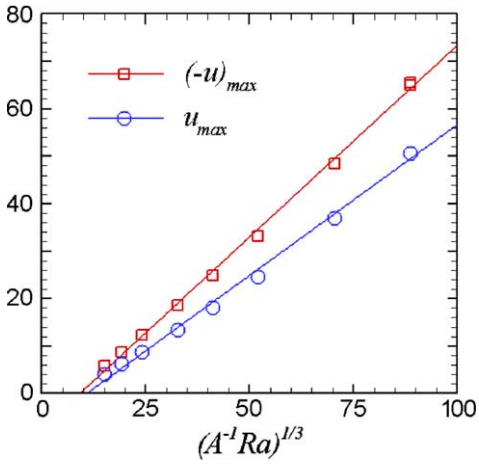

Fig. 7. Maximum flow velocities in the wedge at the steady state (transitional flow regime only). $(-u)_{\max}$ is the maximum velocity in the surface layer and $u_{\max}$ is the horizontal component of the maximum velocity down the slope.

transfer rate for each Rayleigh number, and thus the plotted total heat transfer rate is maintained at a constant value (-1), whereas the plotted convective and conductive heat transfer rates indicate the fractions of the contributions of convection and conduction respectively. It is clear in Fig. 6 that the heat transfer is completely dominated by conduction at very low Rayleigh numbers and by convection at very high Rayleigh numbers. At medium Rayleigh numbers, both conduction and convection contribute to the overall heat transfer. Accordingly, the flow can be classified into three distinct regimes: a low Rayleigh number conductive regime, a medium Rayleigh number transitional regime and a high Rayleigh number convective regime. These three flow regimes, as marked in Fig. 6, are approximately separated by the scales given in (32) and (35).

4.3. Validation of selected scales

In this section, selected scales are validated against the numerical data in order to verify the validity of the previous scaling analysis.

4.3.1. Maximum flow velocity

We consider the velocity scale for the transitional flow regime here. In this flow regime, the surface layer reaches steady state before the vertical temperature gradient is sufficient to allow an instability. The steady state velocity in the surface layer, which is also the maximum flow velocity to be achieved in this layer, is governed by (31). The flow in the surface layer is in the direction flowing into the tip. Correspondingly, we expect that the outflow down the slope will be on the same scale as the inflow along the surface. Fig. 7 plots the calculated maximum flow velocities against $(A^{-1}Ra)^{1/3}$ as suggested by (31) with $(-u)_{\max}$ representing the maximum absolute velocity in the surface layer and $u_{\max}$ representing the horizontal component of the maximum velocity down the slope. It is seen in this figure that $u_{\max}$ is slightly lower than $(-u)_{\max}$, suggesting that the viscous layer along the slope is slightly thicker than the surface layer. It is also clear in Fig. 7 that both plots indicate a linear correlation between the numerical data and the scaling prediction. The slopes of the linear fit curves are respectively 0.81 for the surface flow and 0.64 for the down-slope flow. Both slopes are of the order of unity. Therefore, the maximum flow velocity in the wedge is well represented by (31).

4.3.2. Volumetric flow rate

Again, the transitional flow regime is considered. The steady state volumetric flow rate in this flow regime is governed by (38). It is noteworthy that (38) represents the horizontal exchange rate at the deep end with the absence of the rigid wall there. It is estimated using the maximum flow velocity achievable in the surface layer at the steady state, and it carries an assumption that the flow velocity is uniform across the sectional plane. In the numerical simulations, the volumetric flow rate is calculated using Eq. (46), which account for the actual velocity profile. It is expected that the volumetric flow rates calculated from the numerical data are lower than the scaling prediction $(Ra/8A)^{1/3}$. They are compared in Fig. 8, which plots the numerical results against the scaling prediction. This figure indicates a clear linear correlation between the numerical data and the scaling prediction. The slope of the linear fit curve is 0.19, which is of the order of unity. This result verifies the scaling prediction with respect to the steady state flow rate (the scale (38)).

4.3.3. Critical time for the onset of convective instability

According to the scaling given in Section 2.2, the convective instability presents in the convective flow regime

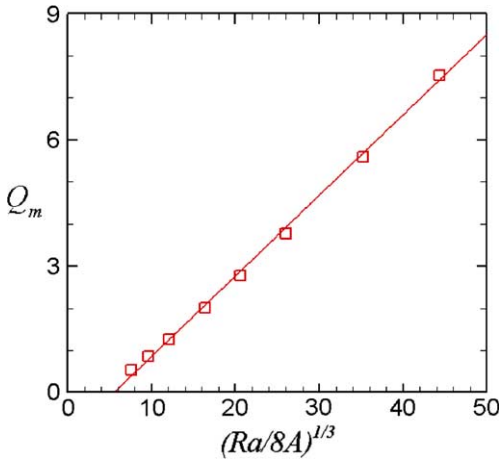

Fig. 8. Integrated mean volumetric flow rate at the steady state (transitional flow regime only).

for $Ra > A^4 Ra_c^3$ and the critical time scale for the onset of the instability is t_B given by (33). This scale is validated here, where the critical Rayleigh number is $Ra_c = 657.5$. The critical time for the onset of the convective instability may be accurately determined from a direct stability analysis based on three-dimensional calculations of perturbed flows (refer to Lei and Patterson, 2003). In the present two-dimensional calculations, the critical time is determined in a similar way.

First, we plot the horizontal temperature profiles in the surface layer. Typical temperature profiles obtained along the first grid line away from the water surface for $Pr = 7$, $Gr = 10^6$ and $A = 0.1$ are given in Fig. 9a. In the shallow end, the isotherms are predominantly vertical as conduction dominates the heat transfer, and instability will not occur; in the deep end, the vertical flow induced by the end-wall will introduce additional effects. Therefore, only the central part of the surface layer ($x = 3$–8) is relevant to the demonstration of the onset of instability. Fig. 9a shows that the temperature in the surface layer is uniform at $t = 0.005$ and 0.01. As time goes on, a clear wave pattern appears at $t = 0.0125$, indicating the presence of the convective instability. The horizontal wave pattern associated is further amplified at $t = 0.015$. The strength of the instability may be measured by the standard deviation of the temperature about its mean value. Fig. 9b plots the time history of the standard deviation calculated from the temperature profiles given in Fig. 9a. The critical time t_B for the onset of the convective instability can be clearly identified from this plot. This is indicated in Fig. 9b. It is seen in Fig. 9b that the standard deviation of temperature is close to zero for $t < t_B$, suggesting that the surface layer is stable. For $t > t_B$, the standard deviation increases rapidly, indicating the presence of the convective instability. Therefore, $t = t_B$ is the critical point when the instability starts to occur.

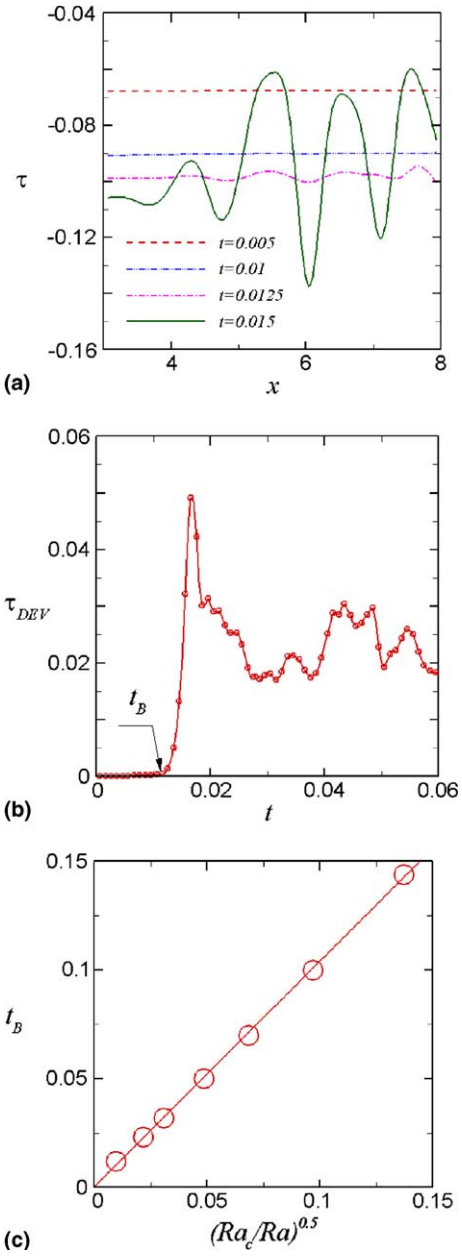

Fig. 9. (a) Calculated temperature profiles in the surface layer ($Pr = 7$, $Gr = 10^6$ and $A = 0.1$). (b) Time history of the standard deviation calculated from the temperature profiles given in (a). (c) Calculated critical time for convective instability against the scaling prediction.

The critical times for the onset of the convective instability determined with the above-mentioned procedures for a range of Ra values are plotted against the scaling prediction in Fig. 9c. This plot clearly indicates a linear correlation between the calculated t_B and that predicted by scaling. The slope of the linear fit curve in Fig. 9c is very close to unity, which verifies the scaling result. Therefore, the critical time for the onset of the convective instability is properly represented by (33).

4.4. Discussion

The validation of the scaling by the numerical analysis may be questioned on the basis of the applicability of the numerical procedures to the model of the coastal waters of lakes and reservoirs. There are two particular issues relevant: the applicability of a two dimensional numerical simulation to the model, and the presence of the end wall at the deep end of the triangular cavity.

4.4.1. Validity of the two-dimensional simulations

The flow in the model region is assumed, in the initial stages, to be two-dimensional. This is a valid assumption in the context of the geophysical application, where the alongshore length scales are usually very much longer than those in the vertical or on shore directions. The assumption means that the scales may not be valid for shorelines with complex alongshore geometry. Those applications will require an extended study. Even with these exclusions, the presence of instabilities generated by surface cooling means that the flow becomes three-dimensional. The scaling analysis stops short of discussing the properties of the instabilities, but does predict the time scale of and the conditions for their occurrence, which arise from the two-dimensional part of the flow.

Under this assumption therefore, the scaling and the numerical analysis up until the point where the instabilities actually form is valid. As discussed in Lei and Patterson (2003), comparison between the two- and three-dimensional solutions for the surface heating case, which also generated instabilities, showed that the two-dimensional simulations accurately predicted all of the gross features of the flow regardless of its three-dimensional nature. Naturally, the details of the falling plumes and their interactions with the bottom flow will require an additional study that is beyond the scope of the present paper which is focused on the scales appropriate for the developing flow.

4.4.2. Effects of the end-wall

The numerical analysis assumes the presence of a vertical end-wall at the deep end of the cavity, in common with the previously cited related papers (Farrow and Patterson, 1993a; Horsch et al., 1994; Lei and Patterson, 2002c). The scaling analysis takes no account of the presence of a rigid wall, consistent with the geophysical application. However, the length scale of the cavity does enter the scaling through the calculation of horizontal pressure gradients resulting from both the Phillips mechanism (18) and (19) and unequal heat capture (26). In both cases, the length is relevant only in the sense that it is the region over which the forcing is applied, that is the length over which the bottom slope is present. A more realistic model of the nearshore region would perhaps continue the domain horizontally, at a constant depth. In that case, the scaling for the development of the flow would be identical since the length scale for the forcing would remain the length of the region over which the bottom sloped.

The influence of the wall is therefore confined to a region near the wall where the flow is turned around. Clearly, the time taken for the flow to reach a steady or quasi-steady state will be extended as the result of the increased volume of fluid if the domain is extended horizontally, but the character of the flow in the sloping bottom region will be substantially unaffected. This is confirmed in the recent paper by Farrow (2004) which shows that the asymptotic solutions in the sloping bottom region are virtually identical to computed solutions in the same region, with a rigid end-wall. There may be other effects of the wall which do not affect the character of the developing flow in the main part of the domain; for example, the circulation in the upper corner at the deep end shown in Fig. 4c and d is the result of the interaction of the wall with the main flow but does not significantly influence the interior flow.

5. Conclusions

The present study has considered the unsteady natural convection in a wedge induced by surface cooling. The fluid in the wedge is initially isothermal and stationary. A constant heat loss is imposed instantaneously at the water surface and maintained thereafter. The flow response to the sudden cooling is then investigated through combined scaling and numerical procedures. The scaling analysis has identified two important flow mechanisms that drive a circulation in the wedge. The first of these is the so-called Phillips mechanism. This mechanism is relevant to the adiabatic thermal condition at the sloping bottom, which forces the isotherms to curl over near the slope. The curling over of the isotherms then generates a temperature gradient along the slope, which in turn initiates a circulation. It is understood that the flow driven by the Phillips mechanism is very weak. This mechanism is significant in the absence of external forcing or in the case with weak external forcing (very small Rayleigh numbers). With the presence of strong cooling at the water surface, the contribution of the Phillips mechanism is negligible.

The second mechanism (unequal heat loss) is directly relevant to the changing water depth in the wedge. Heat is diffused from the inner region to the surface layer and eventually lost at the water surface. In the shallow region, the diffusion generates approximately vertical isotherms, indicating that the heat loss through the water surface is uniformly distributed over the local water depth. Since the water depth is not constant, a horizontal temperature gradient is established, which in turn drives a flow in the wedge. The unequal heat loss is

the dominant driving mechanism for the problem considered here.

The flow driven by the unequal heat loss is then investigated. Different flow regimes have been identified through the scaling analysis, and major scales have been established to quantify the flow development. The scaling results have been validated against numerical data. It is revealed that, in the case of $A > Ra_c^{-0.5}$, the laminar flow induced by the surface cooling can be broadly classified into one of the three flow regimes: a conductive regime, a transitional regime and a convective regime, depending on the Rayleigh number. The major features of each flow regime are summarised as follows:

1. *Conductive regime*. For $Ra < A^{-2}$, the flow is purely conductive. The surface layer expands to encompass the entire domain before convection becomes important. At the steady state, the heat loss through the water surface is uniformly distributed over the local depth, and thus approximately vertical isotherms are observed everywhere in the wedge. A weak circulation is maintained at the steady state.
2. *Transitional regime*. For $A^{-2} < Ra < A^4 Ra_c^3$, both conduction and convection participate in the heat transfer. The convection is more or less important depending on the Rayleigh number. The transient flow development is described by the scales (7), (8) and (26). A steady state is reached when the conduction balances the convection in the surface layer at the time scale (28). At the steady state, the surface layer is distinct, and the maximum flow velocity is given by (31).
3. *Convective regime*. For $Ra > A^4 Ra_c^3$, the flow becomes purely convective. The development of the surface layer in the early stage is described by the scales (7), (8) and (26). At the time (33), the Rayleigh–Bénard convection sets in, and the subsequent flow development and approach to steady state become oscillatory. At a certain stage, a quasi-steady state is reached with both the primary convection and a secondary convection coexists.

Similarly, three flow regimes are possible for the other case with $A < Ra_c^{-0.5}$, which shares many features of a horizontal fluid layer cooled at the top. The flow is stable and fully conductive if $Ra < Ra_c$, while it becomes fully unstable in the regime $Ra_c < Ra < A^{-2}$. Further increase of the Rayleigh number will results in a distinct thermal boundary layer developing along the sloping bottom, which is unstable to the Rayleigh–Bénard instability. The flow is fully convective in this high Rayleigh number regime.

It is worth noting that the present study along with its counterpart (Lei and Patterson, 2002c) has demonstrated that the flow development in the wedge subjected to constant heating and cooling through the water surface exhibits many similar features. In both cases, three distinct flow regimes, i.e. conductive, transitional and convective regimes, are identified. The flow structures in each of these three flow regimes are similar for the heating and cooling cases, and the flow development is quantified by similar scales. The heating and cooling through the water surface are the two opposite processes during a diurnal cycle. The understanding of the flow features for these two separate processes will lead to the understanding of the flow development during a full diurnal cycle (with alternative heating and cooling), which is an ultimate objective of the present investigation.

Acknowledgment

This research was funded by the Australian Research Council and supported by James Cook University.

References

Adams, E.E., Wells, S.A., 1984. Field measurements on side arms of Lake Anna Va. Journal of Hydraulic Engineering 110, 773–793.

Farrow, D.E., Patterson, J.C., 1993a. On the response of a reservoir sidearm to diurnal heating and cooling. Journal of Fluid Mechanics 246, 143–161.

Farrow, D.E., Patterson, J.C., 1993b. On the stability of the near shore waters of a lake when subject to solar heating. International Journal of Heat and Mass Transfer 36 (1), 89–100.

Farrow, D.E., Patterson, J.C., 1994. The daytime circulation and temperature structure in a reservoir sidearm. International Journal of Heat and Mass Transfer 37 (13), 1957–1968.

Farrow, D.E., 2004. Periodically forced natural convection over slowly varying topography. Journal of Fluid Mechanics 508, 1–21.

Horsch, G.M., Stefan, H.G., 1988. Convective circulation in littoral water due to surface cooling. Limnology and Oceanography 33 (5), 1068–1083.

Horsch, G.M., Stefan, H.G., Gavali, S., 1994. Numerical simulation of cooling-induced convective currents on a littoral slope. International Journal for Numerical Methods in Fluids 19, 105–134.

Lei, C., Cheng, L., Armfield, S.W., Kavanagh, K., 2000. Separation points and the near wake of a circular cylinder near a plane boundary. Computational Fluid Dynamics Journal 8 (4), 521–535.

Lei, C., Patterson, J.C., 2002a. Natural convection in a reservoir sidearm subject to solar radiation: a two-dimensional simulation. Numerical Heat Transfer, Part A. Applications 42, 13–32.

Lei, C., Patterson, J.C., 2002b. Natural convection in a reservoir sidearm subject to solar radiation: experimental observations. Experiments in Fluids 32 (5), 590–599.

Lei, C., Patterson, J.C., 2002c. Unsteady natural convection in a triangular enclosure induced by absorption of radiation. Journal of Fluid Mechanics 460, 181–209.

Lei, C., Patterson, J.C., 2003. A direct stability analysis of a radiation-induced natural convection boundary layer in a shallow wedge. Journal of Fluid Mechanics 480, 161–184.

Monismith, S.G., Imberger, J., Morison, M.L., 1990. Convective motions in the sidearm of a small reservoir. Limnology and Oceanography 35, 1676–1702.

Phillips, O.M., 1970. On flows induced by diffusion in a stably stratified fluid. Deep-Sea Research 17, 435–443.

Sturman, J.J., Oldham, C.E., Ivey, G.N., 1999. Steady convective exchange flows down slopes. Aquatic Sciences 61, 260–278.

Wunsch, C., 1970. On oceanic boundary mixing. Deep-Sea Research 17, 293–301.